Co3O4/rGO Catalysts for Oxygen Electrocatalysis: On the Role of the Oxide/Carbon Interaction

I. Abidat, E. Cazayus, L. Loupias, C. Morais, C. Comminges, T. Napporn, David Portehault, O. Durupthy, A-S. Mamede, C. Chanéac, et al.

Co_3O_4/rGO catalysts for oxygen electrocatalysis: on the role of the oxide/carbon interaction

I. Abidat[1], E. Cazayus[2], L. Loupias[1], C. Morais[1], C. Comminges[1], T. W. Napporn[1], D. Portehault[2], O. Durupthy[2], A-S. Mamede[3], C. Chanéac[2], J-F. Lamonier[3], A. Habrioux[z,1], K. B. Kokoh[1]

1. Université de Poitiers, IC2MP UMR 7285 CNRS, 4 rue Michel Brunet, TSA 51106, 86073 Poitiers, Cedex 9, France.
2. Sorbonne Université, CNRS, Collège de France, Laboratoire de Chimie de la Matière Condensée de Paris, 4 place Jussieu, F-75005 Paris, France.
3. Univ. Lille, CNRS, Centrale Lille, ENSCL, Univ. Artois, UMR 8181 - UCCS - Unité de Catalyse et Chimie du Solide, F-59000 Lille, France.

[z]Corresponding Author E-mail Address**:** aurelien.habrioux@univ-poitiers.fr

Abstract:
The reduction degree of graphene oxide substrate governs the activity and stability of Co_3O_4/rGO nanocomposites towards oxygen reduction reaction and oxygen evolution reaction. In this work, Co_3O_4 nanoparticles with narrow size distribution were uniformly deposited onto graphene oxide materials with different reduction degrees, by using a microwave-assisted hydrothermal method. The physicochemical characterization of these nanocomposites indicates that oxygenated groups grafted onto a reduced graphene oxide surface allows creating strong interactions between the carbon-based substrate and Co_3O_4 nanocrystals. The obtained results denote that the electrocatalytic activity and stability of these nanocomposites towards the ORR and OER depend on the entanglement between the strength of the carbon/oxide interaction and the electronic conductivity of the substrate.

Introduction

With the ever increasing clean and sustainable energy demand, numerous efforts have been devoted to developing electrochemical energy conversion and storage devices, such as electrolyzers, solar cells or rechargeable metal air batteries due to their high efficiency, cost-effectiveness and environmentally friendly operation. [1, 2] The widespread commercialization and use of these systems is currently hampered by the lack of low cost and stable catalysts able to activate oxygen reduction (ORR) and/or oxygen evolution (OER) reactions at low overpotentials with high charge transfer kinetics. Currently, Pt-based materials are the most efficient ORR catalysts and are widely studied, [3] while combinations of Ir and Ru-based oxides are recognized as the best OER catalysts. [4] Nevertheless, the scarcity of these platinum group metals limits their large-scale application. [5] In addition, these PGM-based catalysts exhibit limited performances as OER/ORR bifunctional catalysts since Pt has a poor activity towards OER, while the ORR exhibits sluggish kinetics at the RuO_2/IrO_2 cathode surface. [6]

Recently, cobalt oxide-graphene derivative composites have attracted much attention in the field of electrochemical energy conversion and storage systems. [7-9] Co-based spinels

have indeed demonstrated a high catalytic activity towards OER in alkaline media. Co-based spinel oxides also exhibit a high stability. [10, 11] For these materials, the potential drop in the space charge region is specifically high at cathodic potentials such as those required for the ORR. To enhance the charge transfer kinetics at the surface of Co-based spinel oxides, a highly electron conductive substrate is required. In this context, reduced graphene oxide (rGO) attracts tremendous attention as substrate for the deposition of cobalt-based catalysts, because of its high electronic conductivity, high specific surface area and corrosion resistance. [12-14] rGO is classically obtained by reducing exfoliated graphite oxide to eliminate oxygen functionalities and partially restore the π-π conjugated network. This process can be performed using various chemical or physical methods. [15, 16] Chemical reduction of graphene oxide is among the most promising routes to produce large amounts of rGO meeting the industrial requirements for electrochemical applications. However, the properties of rGO depend on the chemical nature of the reducing agent. [17] Depending on the reducing treatment, a variety of defects and polar groups at the surface of rGO are observed, thus enabling fine-tuning of the chemical, electrical and physical properties of rGO materials. [17-19] Heterogeneous nucleation of Co_3O_4 particles onto rGO leads to a strong interfacial interaction impacting the activity of the spinel towards OER and ORR. [20] Hence, the catalytic activity and stability of composite materials towards OER and ORR depend strongly on the reduced graphene oxide properties. [21, 22] Nevertheless, the role of the reduction degree of graphene oxide on the electrocatalytic activity of Co_3O_4/rGO nanocomposites and its stability has not been reported, to the best of our knowledge.

The objective of this work is then to unveil the role played by the interaction between rGO and spinel phase as well as by rGO graphitization degree on the activity and stability of Co_3O_4/rGO catalysts towards OER and ORR. For this purpose a novel synthesis pathway towards bifunctional electrocatalytic nanoheterostructures with optimized and well-controlled interfaces was developed. A fully controlled reduction degree of rGO samples was achieved using chemical treatments. Then nanospinels were deposited onto rGO using an innovative soft chemistry approach. This resulted in the formation of model composite catalysts whose fine and in-depth characterization revealed the role played by interfaces towards oxygen electrocatalysis. This led to conclude that OER and ORR kinetics can be described as a balance between strength of the oxide substrate interaction (governed by the amount of remaining oxygenated groups) and the rGO graphitization degree (governing the electronic conductivity) on the OER/ORR activity and stability of graphene supported spinel catalysts. To the best of our knowledge, this kind of study has never been undertaken to explain the activity and long term stability under harsh conditions of rGO supported nanospinels towards OER and ORR.

Experimental

2.1 Materials preparation

2.1.1 Preparation of reduced graphene oxide

Graphite oxide was synthesized from commercial graphite powder (< 20 µm, Sigma Aldrich) according to a modified Hummer's method. [23] As described above, exfoliation processes as well as reduction treatments were adjusted to provide a large range of rGO materials with tuned reduction degree.

Partially reduced graphene oxide (rGO-PR) was prepared using sodium borohydride as

reducing agent. [19, 24] In a typical synthesis procedure, the GO powder was dispersed in ultra-pure water (1 mg mL^{-1}) under ultrasonication for 90 min to obtain a homogeneous graphene oxide suspension. The pH value of this solution was adjusted to 10 by using a 5 wt. % sodium carbonate solution. Then sodium borohydride solution (≥ 96 %, Sigma-Aldrich) was added into the suspension. The concentration of sodium borohydride in the suspension is adjusted to 0.8 wt.%. Afterwards the solution was magnetically stirred and heated in an oil bath at 80 °C for 1 h. Reduced graphene oxide was recovered by centrifugation for 15 min at 7000 rpm and 15 °C, washed with ultra-pure water and dried under air during 24 h at 40 °C

Strongly reduced graphene oxide (rGO-SR) was prepared using an earlier reported method [25]. In a typical procedure, 2 g of as-synthesized GO was suspended into 750 mL of an acetic acid solution (CH_3COOH, 100%, VWR). A brown colloidal solution was obtained and sonicated for 1 h. Then 40 mL of hydroiodic acid (HI, 57 wt. % Merck) was added into the suspension and the mixture was heated to 40 °C for 48 h with constant stirring. The resulting product was recovered by filtration and washed with large amounts of ultra-pure water and acetone, then dried under ambient conditions.

2.1.2 Preparation of cobalt-based catalysts by hydrothermal microwave-assisted method

20 mg of the reduced graphene oxide black powder (rGO-PR or rGO-SR) were dispersed into a 20 mL ethanol:ultrapure water mixture (50:50 in volume) and magnetically stirred for 24 h. The resulting suspension was then sonicated for 1 h to ensure rGO exfoliation. Immediately after sonication, 0.1300 g of cobalt nitrate hexahydrate ($Co(NH_3)_2.6H_2O$, Aldrich) were added under stirring at room temperature, resulting in the supernatant turning from colourless to pink. With the addition of 2.5 mL of ammonia aqueous solution (11 wt. %, Aldrich), a blue-green precipitate immediately appeared, while the supernatant turned green as well. This suspension was placed in a 30 mL borosilicate glass vial suited to an Anton Paar Monowave 300 monomode microwave oven, sealed with PTFE-coated silicon septum. The colloidal suspension was heated at 100 °C during 10 minutes by microwave irradiation (850 W incident power allowing a very fast heating rate to reach 100 °C within a few seconds). The suspension was then cooled to room temperature in a few minutes under air flow. Magnetic stirring was maintained during the heating process and externally by infrared sensor. The measured pressure during heating should not excess 10 bar. The black powder was washed by several cycles of centrifugation (30 min at 29220 g) – redispersion in Milli-Q® water until the supernatant pH was neutral. The powders were then dried during 12 h at 45 °C under vacuum before further characterization.

2.2 Physical characterizations

Raman spectroscopy was carried out using a LabRAM HR 800 UV spectrometer with an excitation laser wavelength of 514.5 nm (He–Ne radiation) or 532 nm. Decomposition of the experimental signal was performed using Fytik software.

Fourier transform infrared spectroscopy (FTIR) measurements on powders were performed with a Thermo Nicolet Nexus spectrometer using KBr as mulling agent.

The materials surface was characterized by X-ray Photoelectron Spectroscopy (XPS) using a Kratos Analytical AXIS $Ultra^{DLD}$ spectrometer. A monochromatic aluminium source (Al Kα =

1486.6 eV) was used for excitation. The analyser was operated in constant pass energy of 20 eV using an analysis area of approximately 700 µm x 300 µm. Charge compensation was applied to compensate for the charging effect occurring during the analysis. The sp^2 C=C C1s (284.5 eV) binding energy (BE) was used as internal reference. Quantification and simulation of the experimental photopeaks were carried out using CasaXPS software. The XPS C 1s spectra of materials was decomposed assuming a Gelius function (A(0.4,0.38,20)GL(20)) for asymmetric lineshape of sp^2 C=C component at BE 284.5 eV (accompanied with the $\pi \rightarrow \pi^*$ transition around 290 eV) and a Gaussian-Lorentzian product (GL(30)) for symmetric lineshape of sp^3 C-C, C-H (285.0 eV), for oxygenated functional groups (C-OH, C-O-C (286.5 eV), C=O (288.0 eV) and O-C=O (289.0 eV)), and for defects in the sp^2 lattice (284.0 eV). [17]
The crystalline structure of cobalt-based catalysts was studied by powder X-ray diffraction (XRD) on a Bruker D8 Advance X-ray diffractometer in the 15-100° 2θ range using a Co Kα X-ray irradiation source (λ= 0.1789 nm). Step time and step size were respectively of 10 s and 0.066°.
Thermogravimetric (TGA) analyses were performed using a DTA-TGA, TA Instruments SDT Q600 apparatus. Experiments were carried out under air with a heating rate of 5 °C min^{-1} from room temperature up to 900 °C. The flow rate was 100 mL min^{-1}.
The morphology and the average size of the particles were analyzed by transmission electron microscopy (TEM) using a Tecnai spirit G2 apparatus equipped with a Gatan CCD and operating at 120 kV (LaB_6). The samples were prepared by evaporating diluted suspensions in ethanol onto carbon-coated copper grids. For the evaluation of the average size of Co_3O_4 particles, more than 200 particles were considered on several TEM pictures.

2.3 Electrochemical characterization

All electrochemical measurements were performed in a conventional three-electrode cell connected to an Autolab PGSTAT 302N bi-potentiostat. A glassy carbon disk electrode (5 mm diameter) was used as the working electrode. A glassy carbon slab and a calibrated Hg/HgO reference electrode (0.927 V *vs*. RHE) filled with 1 mol L^{-1} KOH were respectively used as counter and reference electrodes. Catalytic inks were prepared by mixing 5 mg of catalyst powder, 750 µL ultra-pure water, 250 µL isopropanol and 60 µL Nafion® suspension (5 wt. % in aliphatic alcohols, Aldrich). 8.5 µL of the catalytic ink was dropped onto the working electrode surface and then dried at room temperature under nitrogen atmosphere. Before OER and ORR measurements, cyclic voltammograms were recorded in a nitrogen saturated electrolyte from 0.8 to 1.55 V *vs.* RHE at a scan rate of 50 mV s^{-1}. 50 cycles were needed to stabilize the electrochemical signal. The activity of catalysts towards the OER was evaluated by recording a polarization curve from 1.2 up to 1.8 V *vs.* RHE at a scan rate of 5 mV s^{-1}. These experiments were carried out using a rotating disk electrode purchased from OrigaLys set at a rotation rate of 1600 rpm. All OER polarization curves were corrected for ohmic drop effect, with resistance values obtained from impedance spectroscopy measurements. The ORR activity on the various materials was evaluated in an O_2-saturated electrolyte by recording polarization curves from 1.00 down to 0.25 V *vs*. RHE at different rotation rates (400, 900, 1600, and 2500 rpm) with a scan rate of 5 mV s^{-1}. These experiments were performed using a rotating ring-disk electrode (RRDE) (AFMSRX modulated speed rotator mounted with AFDT22 electrodes, PINE Instrument Company).

The number of electrons exchanged per oxygen molecule (n) during the ORR and the kinetic current density were calculated from the Koutecky–Levich (K–L) equation. [26, 27]
The amount of HO_2^- formed as well as the number of electrons exchanged per oxygen molecule (n) were determined by using the following equations [28]:

$$\%HO_2^- = 200 \times \frac{I_r / N}{I_d + I_r / N} \quad (1)$$

$$n = 4 \times \frac{I_d}{I_d + I_r / N} \quad (2)$$

where I_d is the disk current, I_r is the ring current and N is the collection efficiency of the Pt ring electrode. N was determined as described by Gasteiger et al. [28] and a value of 22.1% was herein obtained. Catalytic performances of commercial IrO_2 (99.9%, Alfa-Aesar) and Pt/C (10 wt %, Johnson Matthey) catalysts toward OER and ORR have been respectively determined for comparison.
OER stability tests were performed using a nickel foam impregnated with a catalytic ink. Catalytic inks were prepared by mixing 8 mg of catalyst powder with 2 mL of a solution composed of a 3:1 v/v ultra-pure water/absolute ethanol mixture. Finally, 60 µL of a PTFE solution (60 wt. % in water, Aldrich) was added to the suspension to facilitate the cohesion of the catalytic layer as well as to increase the hydrophobicity of the deposit, which ensures good removal of oxygen bubbles formed during oxygen evolution. After 30 min sonication, the prepared ink was deposited onto the nickel foam by drop casting method. The long-term stability of composite catalysts was evaluated by chronopotentiometry in a 1 mol L^{-1} KOH electrolyte by applying a current density of 25 mA cm^{-2} during 20 h. Long-term stability of the composite catalysts in an air electrode configuration was evaluated with a home-designed oxygen flow working electrode. A Teflon coated carbon plate was used as a current collector. 10 µL of the catalytic ink already used to perform OER stability tests was deposited onto the Teflon coated carbon fiber paper (the loading amount was 0.2 mg cm^{-2}) and allowed to dry. The stability of electrochemical performances was evaluated using a home-made air electrode in a 6 mol L^{-1} KOH electrolyte by alternatively applying a current density of -10 mA cm^{-2} during 4 h (ORR) and 10 mA cm^{-2} during 4 h (OER). The duration of the stability test was 30 hours.

Results and discussion

3.1 Synthesis and physico-chemical characterizations

Graphene oxide (GO) has been reduced to varying extent: sodium borohydride yields partially reduced GO (rGO-PR) and hydroiodic treatment leads to strongly reduced GO (rGO-SR). In order to identify and quantify residual functional groups on the surface of reduced graphene oxides, the carbonaceous powders were first characterized using X-ray photoelectron and Fourier transform infrared (FTIR) spectroscopies. Figure 1A-C shows the XPS C1s spectra obtained with the different reduced graphene oxides while FTIR spectra are plotted in Figure 1D.

FIGURE 1

The C1s spectrum of GO (Figure 1A) shows that Hummer's method leads mainly to the formation of hydroxyl and/or ether groups at the surface, while about 24% of total carbon remain graphitic. The partial reducing treatment increases the fraction of graphitic structure to 53% (Figure 1B), in agreement with the loss of oxygenated functional groups. Finally the strong reducing treatment allows restoring further the graphitic structure (64%). FT-IR spectroscopy (Figure 1D) enables identifying more precisely the nature of the surface oxygen-containing functional groups for the different carbon-based materials. Briefly, graphene oxide GO contains adsorbed water (O-H stretch: broad band at 3050 – 3600 cm^{-1}), hydroxyl (O-H stretch at 3050 – 3600 cm^{-1}, C-OH bend at 1367 cm^{-1}), carboxylic (O-H stretch at 3050 – 3600 cm^{-1}, C=O stretch at 1730 cm^{-1}, C-OH bend at 1367 cm^{-1}), carbonyl (C=O stretch at 1617 cm^{-1}), [29] ethers/epoxides/esters (C-O stretch and C-O-C stretch at 1053 -1300 cm^{-1}), [30] and epoxide (C-O asymmetric stretch at 850 cm^{-1}) [31] groups. After partial reduction of GO (rGO-PR), the intensities of the bands corresponding to hydroxyl, carboxyl and carbonyl species are strongly weakened, showing the removal of a large fraction of oxygenated groups. Additional bands at 1454 and 1354 cm^{-1} arise from residual carbonates resulted in the reduction process. The broad band at 1557 cm^{-1} for rGO-PR is assigned to sp^2-hybridized C=C in plane vibrations. The spectrum obtained after strong chemical reduction by hydroiodic acid (rGO-SR) shows considerable decrease of O-H bands, which indicates further removal of functional groups. The strong intensity of the C=C skeletal vibration at around 1560 cm^{-1} confirms the removal of out-of-plane oxygen species and recovery of the sp^2 network.

Raman spectra of the different graphene-based substrates before and after cobalt oxide deposition are shown in Figure 2A-C in the 800-1900 cm^{-1} spectral range. To perform the decomposition of Raman spectra, five lines were considered: [32, 33] two lorentzian lineshapes located at ca. 1350 cm^{-1} (D-line) and 1590 cm^{-1} (G-line) [34, 35]and three gaussian lineshapes centered at ca. 1180 cm^{-1} (D*-line) [36], 1530 cm^{-1} (D″-line) [34] and 1620 cm^{-1} (D′-line). [37] The G mode is attributed to the first-order scattering of the E_{2g} mode. [38] The D mode is a defect-induced one associated with the disruption of the C=C ring structure. [39] In addition, the D" mode is associated with the presence of amorphous sp^2 phase [40, 41] and can be considered as a measurement of the interstitial disorder along the c-axis in these materials containing few stacked graphene layers. This peak is more intense for GO indicating a less pronounced crystallinity of this material along the c-axis in comparison with reduced graphene oxide samples. D* mode has been attributed to the presence of polyenes (polyunsaturated carbon chains) formed subsequently to the grafting of oxygen functional groups on the carbon backbone. [40] The evolution of this mode magnitude with reduction degree is in agreement with conclusions drawn from XPS and FTIR data. Finally, the decrease in the magnitude of D" modes as the reduction degree increases, shows that interstitial disorder between graphene sheets is lowered (better alignment of graphene planes, removal of amorphous sp^2 phases, removal of interstitial atoms,…) by chemical treatments aiming at reducing the surface of the carbon-based materials. The best fits (Table 1) were used to provide more qualitative insights into rGO functionalization.

FIGURE 2

Figure 2: Raman spectra recorded with the different graphene-based substrates: A) GO, B) rGO-PR and C) rGO-SR; (a) without Co_3O_4, (b) after Co_3O_4 deposition. Experimental points are symbolized using brown scatters. Data obtained from decomposition of experimental signals re symbolized using solid lines. D) Raman spectra recorded with the different Co-based nanocomposites: (a) Co_3O_4/GO, (b) Co_3O_4/rGO-PR, (c) Co_3O_4/rGO-SR.

Full widths at half maxima (FWHM) of D and G lines decrease as the reduction degree of graphene oxide increases reflecting an increase of the ordering degree for the most reduced samples. No significant shift of the G-line position is observed. Its value at ca. 1590 cm^{-1} is slightly higher than for highly ordered graphitic structures. As a result, even for strongly reduced sample, the long-range order of perfect graphene is not completely restored by the reducing treatment. The integrated intensity ratio of D- to G-lines, denoted A_D/A_G, allows evaluating the graphitization degree of a carbonaceous material. [33] This ratio is used to quantify the amount of defects and to calculate the in-plane crystallite size (L_a). It is consequently an indirect measurement of the interdefects distance. According to calculated L_a values reported in Table 1, the in-plane crystallite size slightly increases as the reduction degree of graphene oxide increases. This indicates that the size of sp^2 clusters presenting a long-range order is enhanced by reducing treatments, although defects and especially holes formed in the carbon matrix subsequently to the oxidation process remain after reduction processes, as shown by the low L_a values. Therefore, the extension of ordered graphitic domains is only slightly increased upon reduction but the connectivity between these domains is restored. Electronic conduction is enhanced by such connectivity and should then be improved by reduction treatments. As a result of the different physico-chemical investigations carried out with the different materials, properties of carbon-based substrates and supported catalysts can be summarized according to Scheme 1.

SCHEME 1

Scheme 1 shows the disappearance of numerous oxygenated groups thanks to the reducing treatment as well as the partial restoration of the π-conjugated network. Nevertheless, the reducing treatment is not capable of removing holes formed in the carbon backbone during the oxidation of graphite. Moreover, Raman spectra clearly show that corresponding components of G-line and D-line of the various nanocomposites are broader in comparison to those of graphene-based substrates. This broadening effect is associated with the growth of oxide particles onto the substrate that induces a shortening of phonon lifetimes for these two modes. It should be noticed that this broadening is more pronounced for GO and rGO-PR materials which could suggest a stronger interaction of Co_3O_4 oxide with these two substrates than with rGO-SR. From calculated L_a values, it can also be stated that in-plane crystallite size values are slightly affected by oxide deposition for GO and rGO-PR since they vary from 5.4 and 6.3 to 4.5 and 5.0 nm for Co_3O_4/GO, Co_3O_4/rGO-PR samples, respectively. For rGO-SR the interdefects distance between long-range ordered sp^2 domains is not affected by oxide nucleation. Hence, particles are either weakly interacting with these domains or they are mainly growth onto structural defects.

TABLE 1

Raman spectroscopy is also an efficient tool for studying local structure of transition metal oxides, in particular cation distribution, effects of phase transition, oxygen disorder effects and microstrain affecting the oxide lattice. The Raman spectra of the three Co-based nanocomposites are plotted in Figure 2D. For the three studied materials, the five observed lines correspond to the five Raman active phonon modes (A1g+Eg+3F2g) expected for the normal spinel structure Co_3O_4. [42] Compared to those of the single-crystal material, these lines are broader and red-shifted which may be explained by particle size or strain effects. Additionally, the lines observed in the Co_3O_4/GO Raman spectrum were found to be slightly broader which could be related to a higher oxygen disorder. This could probably be explained by the stronger interaction with the support that may result in defects in the oxygen sublattice, which would shorten the phonon modes lifetime and therefore broaden the Raman lines

Figure S1 shows the typical XPS Co 2p spectrum and powder X-ray diffraction patterns recorded at room temperature for cobalt-based composites synthesized in this study. For all these samples, diffraction patterns (Figure S1A) can be indexed to the cubic spinel lattice (Fd-3m space group) according to the standard JCPDS file (JCPDS file number 80-1544). No crystallized secondary phase could be detected. For all samples, the lattice parameter value of the spinel phase is ca. 8.09 Å. The average size of coherently diffracting domains determined using Scherrer equation are of 9.6, 8.5 and 10 nm for Co_3O_4/GO, Co_3O_4/rGO-PR and Co_3O_4/rGO-SR, respectively. The diffraction line centered at ca. 28° (2theta) for Co_3O_4/rGO-SR is assigned to the interlayer (002) plane of the hexagonal lattice of graphite. [43] The intensity of this peak is much more pronounced using strongly reduced graphene oxide as substrate. This confirms the long range order along the c-axis of graphitic lattice with the stacking of several graphene layers. The broadness of the peak is associated with the presence of nanographitic clusters composed of stacks of few graphene layers. For Co_3O_4/GO and Co_3O_4/rGO-PR, this peak cannot be identified due to the presence of numerous oxygenated groups, which hinder the stacking of the carbonaceous sheets and lead to a strongly disordered material along the c axis. Note that this peak for Co_3O_4/rGO-SR may also arise from partial restacking of the dispersed rGO sheets during drying of the suspensions.

The XPS Co 2p spectrum of Co_3O_4/GO (Figure S1B) shows the spectral fingerprint of Co_3O_4. Indeed, the main Co $2p_{3/2}$ photopeak (BE = 779.8 eV) looks asymmetric due to the multiplet splittings [44] of both Co^{3+} and Co^{2+} present in the spinel oxide accompanied with a satellite (SAT) structure at higher BE value (BE = 789.7 eV). [44] Whatever the reducing treatment of the carbon-based substrates, the XPS analyses revealed this same chemical environment for cobalt (Figure S1B and Figure S2). Otherwise, the XPS depth resolution (less than 10 nm) and the high loading rate of Co oxide do not allow probing the graphene-based substrate.

The spinel particle size distribution and dispersion of the Co_3O_4/GO, Co_3O_4/rGO-PR and Co_3O_4/rGO-SR samples were analyzed by Transmission Electron Microscopy (TEM). Figure 3 shows roughly spherical nanoparticles anchored exclusively onto the surface of the carbonaceous sheets. Only few isolated oxide particles can be observed in the Co_3O_4/GO sample. In addition, the nanoparticles are homogeneously dispersed on the surface of the GO or rGO sheets. The edges of the sheets are not privileged nucleation points for Co_3O_4

nanoparticles and very few oxide aggregates are observed in the three composites. Lattice fringes on the nanoparticles confirm the formation of Co_3O_4 (Figure 3H). The average size of the particles determined from TEM analyses corresponds to the size of the crystallites calculated from XRD patterns for all three samples (see Figure S3, Supporting Information) indicating that the particles are single crystals. The Co_3O_4 particles supported onto rGO-PR are slightly larger than particles supported onto the other substrates. Due to the low contrast associated with carbonaceous sheets, it is difficult to estimate the number of restacked sheets. However, Figure 3F clearly displays edges of few rGO stacked layers, while other composites do not such extended stacks. Eight graphitic layers can be distinguished (Figure 3G), with an interlayer distance of ca. 0.3 nm, in agreement with the 28° (2theta) XRD peak corresponding to a distance of 0.3 nm (Bragg's Law). This extended stacking also supports the higher reduction rate highlighted by XPS, Raman and FTIR spectroscopies.

FIGURE 3

The thermal stability under air of the carbonaceous materials has then been assessed by thermogravimetric analysis (TGA) (Figure 4). Three different mass losses are observed. The first stage from 25 to 100 °C can be ascribed to desorption of physically adsorbed water molecules. The water amount in rGO-SR sample is significantly lower than for rGO-PR and GO materials, in agreement with the decreasing magnitude of -O-H vibrational mode observed from FTIR spectra. It is then mostly probable that the amount of intercalated water between graphene planes of RGO-SR few-layers graphene material is lower. The second weight loss from 110 to 250 °C is related to the loss of functional groups containing labile oxygen atoms such as CO_2, CO and H_2O [39, 45] It is of 34.2%, 11.5% and 2.8% for GO, rGO-PR and rGO-SR, respectively, in agreement with the removal of functional groups highlighted by XPS, Raman and FT-IR spectroscopies. The last weight loss can be associated with carbon combustion. The decomposition temperature determined from TGA curves is 550 °C for GO sample, which is lower than rGO-PR (640 °C) and rGO-SR (680 °C) materials. This suggests that the thermal stability of reduced graphene oxide decreases as the oxygen content increases, as already reported. [46]

FIGURE 4

The thermograms corresponding to Co-based samples exhibit a first weight loss before 250 °C, which magnitude decreases from Co_3O_4/GO, to Co_3O_4/rGO-PR and to Co_3O_4/rGO-SR. After carbon combustion, the remaining mass at 700 °C is used to evaluate the Co_3O_4 mass loading, which is 67, 71 and 63 wt %, for Co_3O_4/GO, Co_3O_4/rGO-PR, and Co_3O_4/rGO-SR, respectively. Hence, the Co_3O_4/carbonaceous ratio is relatively similar for all nanocomposites. Furthermore, carbon combustion occurs at lower temperatures in the presence of cobalt oxide: *ca.* 360 °C for Co_3O_4/GO and Co_3O_4/rGO-PR (vs. 600 and 640 °C, respectively, hence shifting of about 300 °C). This temperature shift is weaker for the most reduced sample (*i.e.* Co_3O_4/rGO-SR), for which combustion occurs at 540 °C (vs. 680 °C for pristine rGO-SR material), thus showing that this composite is largely more resistant to thermal decomposition under air atmosphere. Thermal destabilization of rGO materials in contact with Co_3O_4 particles can be related to the

catalytic effect of Co_3O_4 nanoparticles. [47] Metal centers are indeed capable of catalyzing carbon combustion. [48, 49] Oxygen functional groups grafted onto the graphene derivatives might enhance the interaction between metal oxide and carbon-based substrates through the formation of strong metal substrate interactions (Co-O-C). [22, 50] In other words, oxygen-functional groups tend to act as ligand capable of stabilizing metal centers and thus allowing a strong covalent interaction between cobalt and graphene-based surface to be formed. [51] This latter is responsible for promoting the catalytic carbon combustion reaction. In contrast, the use of strongly reduced substrates leads to the deposition of Co_3O_4 particles on structural defects of reduced graphene oxide. Then, the interaction formed between strongly reduced graphene oxide and cobalt oxide is weaker. [52]

3.2 Electrochemical characterizations

The electrocatalytic activity of the different composite catalysts towards ORR was examined using a conventional three electrodes electrochemical cell with a RRDE working electrode in O_2-saturated 1 mol L^{-1} KOH electrolyte. Figure 5A shows polarization curves recorded at 5 mV s^{-1} using the disk electrode as well as ring currents obtained at a rotation rate of 1600 rpmCo_3O_4/rGO-PR nanocomposite shows the highest catalytic performance towards ORR, with onset and half-wave potentials respectively of 0.87 and 0.77 V vs. RHE. This is clearly higher than those obtained with Co_3O_4/rGO-SR (0.83 and 0.71 V vs. RHE) and Co_3O_4/GO (0.72 and 0.64 V vs. RHE) samples and highlights higher electrocatalytic activity of the nanocomposite with an average reduction level. The low activity of Co_3O_4/rGO-SR in comparison with that of Co_3O_4/rGO-PR can be assigned to the above-mentioned weaker interaction between Co_3O_4 and strongly reduced rGO. This weak interaction is responsible for increasing charge transfer resistance and consequently for limiting the catalyst activity. On the other hand, the activity of Co_3O_4/GO is found to be significantly lower than for Co_3O_4/rGO-PR sample despite the presence of more oxygenated functional groups on the pristine substrate. This activity difference can be related to the low electronic conductivity of graphene oxide that is composed of small and poorly connected graphitic domains, as shown by Raman spectroscopy. Moreover, carbon atom polarization induced by electron withdrawing effects exerted by oxygen atoms grafted onto the carbon based-substrate surface could play an important role on the electronic modification of cobalt oxide, thus changing the nanocomposite activity towards ORR. Tafel slope values which vary from 91 mV dec^{-1} for Co_3O_4/GO down to 55 mV dec^{-1} for Co_3O_4/RGO-PR (Figure S5) provide evidences of changes in the nature or in the kinetics of the rate determining-step. These changes could highlight a modification of the adsorption energies of oxygenated reaction intermediates involved in the ORR process. The percentage of peroxide species formed with respect to total oxygen reduction products as well as the number of electrons exchanged per oxygen molecule (n_{exp}) were determined from measured disk and ring currents. Results are shown in Figure 5B. Whatever the catalyst, the yield of peroxide species formed during the reduction process remains below 10%. This corresponds to electron transfer number in the range of ~3.7 - 4.0 from 0.80 to 0.25 V *vs.* RHE for all catalysts. The obtained values suggest that for all catalysts the reaction mechanism implies a mixed $4e^-$ and $2e^-$ reduction process. As references, RRDE measurements were also realized with the different carbon-based substrates (Figure S4). These materials have poor ORR activities. GO is almost inactive towards ORR and rGO-SR is more active than rGO-PR. The

yields of peroxide species formed during the ORR process are 75 and 55% for RGO-SR and RGO-PR, respectively.

FIGURE 5

Polarization curves were also recorded at different rotation rates in an O_2-saturated 1 mol L^{-1} KOH electrolyte to determine kinetic parameters governing the reduction process at the surface of the different Co-based composites. Figure S6 shows the LSV curves obtained with Co_3O_4/rGO-PR. The limited current density increases with rotation rate, indicating that it is controlled by mass transport. [53] Kinetic current densities were calculated from Koutecky-Levich (K-L) plots. Values obtained at 0.7 V *vs.* RHE confirm the largely higher catalytic activity of Co_3O_4/rGO-PR material. For this latter material the kinetic current density at 0.7 V *vs.* RHE is indeed of 2.74 mA cm^{-2}, almost three times higher than that obtained with Co_3O_4/rGO-SR catalyst (1.16 mA cm^{-2}) and nine times higher than that measured with Co_3O_4/GO sample (0.3 mA cm^{-2}).

In order to study the effect of graphene oxide reduction degree on the activity of Co-based nanocomposites towards OER, polarization curves were first recorded in a N_2-saturated alkaline electrolyte (1 mol L^{-1} KOH) using a RDE set at 1600 rpm in order to quickly remove bubbles formed during the reaction (Figure 6A).

FIGURE 6

As shown in Figure 6A, the overpotential required to drive a current density of 10 mA cm^{-2} for OER, increases from 380 mV for Co_3O_4 /RGO-SR to 395 mV and 415 mV for Co_3O_4 /RGO-PR and Co_3O_4 /GO, respectively. The increase in the catalytic activity with the reduction degree of rGO indicates that the electronic conductivity of the substrate manages the catalytic activity of the composite material towards OER. [54-56] For a strongly reduced substrate, an increase in electronic conductivity leads to a decrease in the charge transfer resistance. [24] Differences in the observed activity order of nanocomposite catalysts towards OER and ORR result from differences in the chemical nature of the active site for these two electrochemical processes. The active sites for the OER are Co(IV) species located at the surface of the nanoparticles. [10] These active species are formed at potentials higher than 1.4 V *vs.* RHE. The coulometry of the Co^{3+}/Co^{4+} redox transition seems to be higher for Co_3O_4/RGO-SR material in the 1.40 – 1.55 V *vs.* RHE potential range. As a result, the energy needed to form these species may be strongly related to the electronic conductivity of the substrate On the other side, the activity of such composite materials towards ORR depends on the electronic density on Co^{2+}/Co^{3+} species which are the major active sites for the ORR (as the contribution of the reduced graphene oxide substrate alone is negligible in our case (Figure S5). [57] In this case, enhanced interaction with the substrate can promote charge transfer at the heterointerface and modify the electron density on the Co^{2+}/Co^{3+} centers. Parameters governing OER kinetics at the electrocatalysts surface were determined in the low overpotential region using Tafel equation ($\eta = a + b \log j$) (Figure 6B). In the frame of Tafel approximation a Tafel slope of 63 mV dec^{-1} was obtained for Co_3O_4 /RGO-SR. This value is characteristic of a reaction mechanism whose rate determining step is the first electron transfer. [58] The Tafel slope increases from 83 up to 96 mV dec^{-1} for Co_3O_4 /GO

and Co_3O_4/RGO-PR, respectively. The increase in this slope value can be ascribed to a complex electrochemical process involving several electrochemical reactions occurring both on carbon and oxide, implying thus a multi-electron transfer process that includes the OER but may also correspond to the removal of oxygen functionalities from the carbon surface. OER as well as ORR activity of our catalysts can be easily compared with those of both noble metal-based catalysts and other rGO supported cobaltite catalysts (Table S1).

In order to evaluate the stability of catalysts, 20 h long chronopotentiometric experiments were performed at a constant current density of 25 mA cm^{-2}. As shown in Figure 6C, all samples are subjected to a potential increase during 30 min. After this first event, the electrode potential was observed to be nearly constant for Co_3O_4/GO and Co_3O_4/rGO-PR materials. An increase of the potential value with a magnitude of only a few millivolts is then observed, thus showing that the catalyst activity is stable. In contrast, an activity loss continues in a less pronounced way during the remaining time of the test for the Co_3O_4/rGO-SR material. Such an evolution may result from detachment or coalescence of cobalt oxide particles in reason of the already mentioned weak interaction between oxide particles and rGO-SR sheets. In order to confirm this degradation mechanism hypothesis, cyclic voltammograms were recorded before and after 1000 voltammetric cycles between 0.8 and 1.7 V *vs.* RHE (accelerated ageing test) with all investigated catalysts (Figure S7). For Co_3O_4/RGO-SR (Figure S7A), a strong loss in the coulometry associated with redox transitions involving Co atoms is observed. This clearly shows a severe decrease in the cobalt active surface area. In the same time it can be observed that the capacitive behavior remains nearly the same, providing evidences that the loss of carbon, subsequent to a corrosion phenomenon, is negligible. For the two other catalysts (Figure S7B and Figure S7C) no loss in the cobalt oxide active surface area can be observed and the capacitive behavior of the electrode remains unchanged upon electrochemical cycling. This proves that phenomena responsible for the ageing of electrodes composed of Co_3O_4/GO and Co_3O_4/rGO-PR materials occur in a different way than for Co_3O_4/RGO-SR. As conclusive remark, the weak interaction between strongly reduced graphene oxide and cobaltite does not affect its activity towards OER, but strongly limits its stability, whereas the strong interaction formed between oxide particles and RGO-PR or GO substrates allows maintaining the stability for composite catalysts. In order to evaluate the ability of using such catalyst as air electrode, stability tests were carried out by alternatively performing OER and ORR at the catalyst surface. The most active and stable composite catalyst (*i.e.* Co_3O_4/rGO-PR) was selected for this test. The test was carried out in a 6 mol L^{-1} KOH electrolyte by alternatively applying a current density of -10 mA cm^{-2} during 4 h and a current density of 10 mA cm^{-2} during 4 h. Results are shown in Figure 7.

FIGURE 7

The as-obtained results indicate that no ORR activity loss occurs during the test. Nevertheless a slight OER activity loss is observed. The initial OER potential is *ca.* 1.57 V vs. RHE and only of *ca.* 1.60 V vs. RHE after 27 h testing. The electrode potential difference between ORR and OER is initially of 820 mV and slowly rises to 850 mV after 30 h testing. The reversibility loss (of about 3.7%) is therefore very weak after 30 hours test

Conclusions

Graphene oxide materials presenting gradual reduction degrees were prepared via chemical reduction of graphite oxide. The physical characterizations of these graphene-based materials using XPS, IR, ATG and Raman spectroscopy techniques confirmed that the oxygen containing groups and the graphitization degree of these graphene based materials were successfully controlled by tuning the chemical nature of the reducing agent. The microwave-assisted hydrothermal method was shown to be an efficient way to successfully deposit Co_3O_4 nanoparticles through heterogeneous nucleation process onto these graphene-based substrates. This novel synthesis pathway allowed obtaining bifunctional electrocatalytic nanoheterostructures with optimized interfaces. It was shown that as-deposited spinel cobalt oxide nanoparticles exhibited the same size whatever the substrate material used. Raman spectroscopy and thermogravimetric characterizations indicated that the presence of residual oxygen groups in graphene-based substrate induced the formation of a strong oxide substrate interaction in the Co_3O_4/rGO-PR and Co_3O_4/GO samples. In the case of the Co_3O_4/rGO-PR composite, this strong interaction coupled with the high electronic conductivity of the substrate promotes its electroactivity towards the ORR. The electroactivity of the different composites towards OER strongly depends on the graphitization degree of the graphene-based substrate. As a result, Co_3O_4/rGO-SR is the most efficient catalyst towards OER. However, the weak interaction between Co_3O_4 nanoparticles and rGO-SR affects the stability of the corresponding composite that exhibits cobalt leaching. The composite prepared by deposition of Co_3O_4 nanoparticles onto the rGO-PR substrate, which presents a balance between the amount of grafted oxygenated groups and graphitization degree, exhibits the highest performance as bifunctional catalyst. The overpotential required to reach a current density of 10 mA cm^{-2} for OER is of 395 mV. The ORR onset and half-wave potential are 0.87 and 0.77 V vs. RHE, respectively. In addition, this catalyst presents a very high stability since it retains 96% of its initial reversibility criterion (difference between the potential value required to reach 10 mA cm^{-2} during OER and potential value required to drive -10 mA cm^{-2} during ORR) after 30 h testing in at 6 mol L^{-1} KOH electrolyte. This work provides an important contribution for the development of oxide/carbon composites that are promising candidates for the elaboration of a stable and truly reversible air electrode in alkaline media for energy conversion and storage devices. Additionally, the facile synthesis approach allowing a strong physical/chemical attachment of oxide particles onto graphene derivatives can lead to a synergistic coupling between pseudocapacitive properties of spinel oxides and supercapacitive properties of graphene derivatives. This is then of utmost importance for the implementation of most efficient supercapacitors. In this way, this work can have a large impact beyond the electrocatalysis research field.

Acknowledgments

This work was supported by the Agence Nationale de la Recherche (ANR), project E Air (ANR-14-CE05-0036-01). I. Abidat and E. Cazayus are grateful for this financial support (PhD

grants). The *Fonds Européen de Développement Régional* (FEDER), *CNRS*, *Région Nord Pas-de-Calais* and *Ministère de l'Education Nationale de l'Enseignement Supérieur et de la Recherche* are acknowledged for fundings of XPS/LEIS/ToF-SIMS spectrometers within the Pôle Régional d'Analyses de Surface

References

1. E. Fabbri, A. Habereder, K. Waltar, R. Kötz and T. J. Schmidt,"Developments and perspectives of oxide-based catalysts for the oxygen evolution reaction," *Catal. Sci. Technol.*, **4**, 3800 (2014).
2. O. Gröger, H. A. Gasteiger and J.-P. Suchsland,"Review—Electromobility: Batteries or Fuel Cells?," *J. Electrochem. Soc.*, **162**, A2605 (2015).
3. Y. Holade, N. Sahin, K. Servat, T. Napporn and K. Kokoh,"Recent Advances in Carbon Supported Metal Nanoparticles Preparation for Oxygen Reduction Reaction in Low Temperature Fuel Cells," *Catalysts*, **5**, 310 (2015).
4. T. Audichon, T. W. Napporn, C. Canaff, C. Morais, C. Comminges and K. B. Kokoh,"IrO_2 Coated on RuO_2 as Efficient and Stable Electroactive Nanocatalysts for Electrochemical Water Splitting," *J. Phys. Chem. C*, **120**, 2562 (2016).
5. X. Yu and S. Ye,"Recent advances in activity and durability enhancement of Pt/C catalytic cathode in PEMFC," *J. Power Sources*, **172**, 145 (2007).
6. S. Mao, Z. Wen, T. Huang, Y. Hou and J. Chen,"High-performance bi-functional electrocatalysts of 3D crumpled graphene–cobalt oxide nanohybrids for oxygen reduction and evolution reactions," *Energ. Environ. Sci.*, **7**, 609 (2014).
7. R. Raccichini, A. Varzi, S. Passerini and B. Scrosati,"The role of graphene for electrochemical energy storage," *Nat. Mater.*, **14**, 271 (2015).
8. D. Higgins, P. Zamani, A. Yu and Z. Chen,"The application of graphene and its composites in oxygen reduction electrocatalysis: a perspective and review of recent progress," *Energ. Environ. Sci.*, **9**, 357 (2016).
9. C. Li, X. Han, F. Cheng, Y. Hu, C. Chen and J. Chen,"Phase and composition controllable synthesis of cobalt manganese spinel nanoparticles towards efficient oxygen electrocatalysis," *Nat. Commun.*, **6**, 7345 (2015).
10. I. Abidat, N. Bouchenafa-Saib, A. Habrioux, C. Comminges, C. Canaff, J. Rousseau, T. W. Napporn, D. Dambournet, O. Borkiewicz and K. B. Kokoh,"Electrochemically induced surface modifications of mesoporous spinels (Co_3O_{4-d}, $MnCo_2O_{4-d}$, $NiCo2O_{4-d}$) as the origin of the OER activity and stability in alkaline medium," *J. Mater. Chem. A*, **3**, 17433 (2015).
11. L. Wu, Q. Li, C. H. Wu, H. Zhu, A. Mendoza-Garcia, B. Shen, J. Guo and S. Sun,"Stable Cobalt Nanoparticles and Their Monolayer Array as an Efficient Electrocatalyst for Oxygen Evolution Reaction," *J. Am. Chem. Soc.*, **137**, 7071 (2015).
12. A. Ambrosi, C. K. Chua, A. Bonanni and M. Pumera,"Electrochemistry of graphene and related materials," *Chem. Rev.*, **114**, 7150 (2014).
13. J. Xu, Y. Wang and S. Hu,"Nanocomposites of graphene and graphene oxides: Synthesis, molecular functionalization and application in electrochemical sensors and biosensors. A review," *Microchim. Acta*, **184**, 1 (2016).

14. Q. Wu, L. Yang, X. Wang and Z. Hu,"From Carbon-Based Nanotubes to Nanocages for Advanced Energy Conversion and Storage," *Acc. Chem. Res.*, **50**, 435 (2017).
15. W. Choi, I. Lahiri, R. Seelaboyina and Y. S. Kang,"Synthesis of Graphene and Its Applications: A Review," *Crit. Rev. Solid State Mater. Sci.*, **35**, 52 (2010).
16. R. K. Singh, R. Kumar and D. P. Singh,"Graphene oxide: strategies for synthesis, reduction and frontier applications," *RSC Adv.*, **6**, 64993 (2016).
17. I. Abidat, C. Morais, S. Pronier, N. Guignard, J. D. Comparot, C. Canaff, T. W. Napporn, A. Habrioux, A. S. Mamede, J. F. Lamonier and K. B. Kokoh,"Effect of gradual reduction of graphene oxide on the CO tolerance of supported platinum nanoparticles," *Carbon*, **111**, 849 (2017).
18. C. K. Chua and M. Pumera,"Chemical reduction of graphene oxide: a synthetic chemistry viewpoint," *Chem. Soc. Rev.*, **43**, 291 (2014).
19. D. Luo, G. Zhang, J. Liu and X. Sun,"Evaluation Criteria for Reduced Graphene Oxide," *J. Phys. Chem. C*, **115**, 11327 (2011).
20. C. Sun, F. Li, C. Ma, Y. Wang, Y. Ren, W. Yang, Z. Ma, J. Li, Y. Chen, Y. Kim and L. Chen,"Graphene–Co_3O_4 nanocomposite as an efficient bifunctional catalyst for lithium–air batteries," *J. Mater. Chem. A*, **2**, 7188 (2014).
21. J. E. Kim, J. Lim, G. Y. Lee, S. H. Choi, U. N. Maiti, W. J. Lee, H. J. Lee and S. O. Kim,"Subnanometer Cobalt-Hydroxide-Anchored N-Doped Carbon Nanotube Forest for Bifunctional Oxygen Catalyst," *ACS Appl. Mater. Int.*, **8**, 1571 (2016).
22. O. Mabayoje, M. Seredych and T. J. Bandosz,"Cobalt (hydr)oxide/graphite oxide composites: importance of surface chemical heterogeneity for reactive adsorption of hydrogen sulfide," *J. Colloid Int. Sci.*, **378**, 1 (2012).
23. D. C. Marcano, D. V. Kosynkin, J. M. Berlin, A. Sinitskii, Z. Sun, A. Slesarev, L. B. Alemany, W. Lu and J. M. Tour,"Improved synthesis of graphene oxide," *ACS Nano*, **4**, 4806 (2010).
24. W. Gao, L. B. Alemany, L. Ci and P. M. Ajayan,"New insights into the structure and reduction of graphite oxide," *Nat. Chem.*, **1**, 403 (2009).
25. I. K. Moon, J. Lee, R. S. Ruoff and H. Lee,"Reduced graphene oxide by chemical graphitization," *Nat. Commun.*, **1**, 73 (2010).
26. C. Coutanceau, M. J. Croissant, T. Napporn and C. Lamy,"Electrocatalytic reduction of dioxygen at platinum particles dispersed in a polyaniline film," *Electrochim. Acta*, **46**, 579 (2000).
27. Y. Holade, R. G. da Silva, K. Servat, T. W. Napporn, C. Canaff, A. R. de Andrade and K. B. Kokoh,"Facile synthesis of highly active and durable PdM/C (M = Fe, Mn) nanocatalysts for the oxygen reduction reaction in an alkaline medium," *J. Mater. Chem. A*, **4**, 8337 (2016).
28. U. A. Paulus, T. J. Schmidt, H. A. Gasteiger and R. J. Behm,"Oxygen reduction on a high-surface area Pt/Vulcan carbon catalyst: a thin-film rotating ring-disk electrode study," *J. Electroanal. Chem.*, **495**, 134 (2001).
29. T. Szabó, O. Berkesi, P. Forgó, K. Josepovits, Y. Sanakis, D. Petridis and I. Dékány,"Evolution of Surface Functional Groups in a Series of Progressively Oxidized Graphite Oxides," *Chem. Mater.*, **18**, 2740 (2006).
30. J. F. Marco, J. R. Gancedo, M. Gracia, J. L. Gautier, E. Ríos and F. J.

Berry,"Characterization of the Nickel Cobaltite, $NiCo_2O_4$, Prepared by Several Methods: An XRD, XANES, EXAFS, and XPS Study," *J. Solid State Chem.*, **153**, 74 (2000).
31. M. Acik, G. Lee, C. Mattevi, M. Chhowalla, K. Cho and Y. J. Chabal,"Unusual infrared-absorption mechanism in thermally reduced graphene oxide," *Nat. Mater.*, **9**, 840 (2010).
32. R. Hawaldar, P. Merino, M. R. Correia, I. Bdikin, J. Gracio, J. Mendez, J. A. Martin-Gago and M. K. Singh,"Large-area high-throughput synthesis of monolayer graphene sheet by Hot Filament Thermal Chemical Vapor Deposition," *Sci. Rep.*, **2**, 682 (2012).
33. S. Claramunt, A. Varea, D. López-Díaz, M. M. Velázquez, A. Cornet and A. Cirera,"The Importance of Interbands on the Interpretation of the Raman Spectrum of Graphene Oxide," *J. Phys. Chem. C*, **119**, 10123 (2015).
34. T. Jawhari, A. Roid and J. Casado,"Raman spectroscopic characterization of some commercially available carbon black materials," *Carbon*, **33**, 1561 (1995).
35. E. F. Antunes, A. O. Lobo, E. J. Corat, V. J. Trava-Airoldi, A. A. Martin and C. Veríssimo,"Comparative study of first- and second-order Raman spectra of MWCNT at visible and infrared laser excitation," *Carbon*, **44**, 2202 (2006).
36. X. M. Tang, J. Weber, S. N. Mikhailov, C. Müller, W. Hänni and H. E. Hintermann,"Structure stability of hydrogenated amorphous carbon film during thermal annealing," *J. Non-Cryst. Solids*, **185**, 145 (1995).
37. V. Mennella, G. Monaco, L. Colangeli and E. Bussoletti,"Raman spectra of carbon-based materials excited at 1064 nm," *Carbon*, **33**, 115 (1995).
38. F. Tuinstra and J. L. Koenig,"Raman Spectrum of Graphite," *J. Chem. Phys.*, **53**, 1126 (1970).
39. D. Yang, A. Velamakanni, G. Bozoklu, S. Park, M. Stoller, R. D. Piner, S. Stankovich, I. Jung, D. A. Field, C. A. Ventrice and R. S. Ruoff,"Chemical analysis of graphene oxide films after heat and chemical treatments by X-ray photoelectron and Micro-Raman spectroscopy," *Carbon*, **47**, 145 (2009).
40. M. Veres, S. Tóth and M. Koós,"New aspects of Raman scattering in carbon-based amorphous materials," *Diamond Relat. Mater.*, **17**, 1692 (2008).
41. L. G. Cancado, A. Jorio, E. H. Ferreira, F. Stavale, C. A. Achete, R. B. Capaz, M. V. Moutinho, A. Lombardo, T. S. Kulmala and A. C. Ferrari,"Quantifying defects in graphene via Raman spectroscopy at different excitation energies," *Nano Lett.*, **11**, 3190 (2011).
42. I. Abidat, C. Morais, C. Comminges, C. Canaff, J. Rousseau, N. Guignard, T. W. Napporn, A. Habrioux and K. B. Kokoh,"Three dimensionally ordered mesoporous hydroxylated $Ni_xCo_{3-x}O_4$ spinels for the oxygen evolution reaction: on the hydroxyl-induced surface restructuring effect," *J. Mater. Chem. A*, **5**, 7173 (2017).
43. J. B. Aladekomo and R. H. Bragg,"Structural transformations induced in graphite by grinding: Analysis of (002) X-ray diffraction line profiles," *Carbon*, **28**, 897 (1990).
44. M. C. Biesinger, B. P. Payne, A. P. Grosvenor, L. W. M. Lau, A. R. Gerson and R. S. C. Smart,"Resolving surface chemical states in XPS analysis of first row transition metals, oxides and hydroxides: Cr, Mn, Fe, Co and Ni," *Appl. Surf. Sci.*, **257**, 2717 (2011).
45. S. Park, J. An, R. D. Piner, I. Jung, D. Yang, A. Velamakanni, S. T. Nguyen and R. S. Ruoff,"Aqueous Suspension and Characterization of Chemically Modified Graphene Sheets," *Chem. Mater.*, **20**, 6592 (2008).
46. S. Sandoval, N. Kumar, A. Sundaresan, C. N. Rao, A. Fuertes and G. Tobias,"Enhanced

thermal oxidation stability of reduced graphene oxide by nitrogen doping," *Chem. Eur. J.*, **20**, 11999 (2014).
47. C. Xu, X. Wang, J. Zhu, X. Yang and L. Lu,"Deposition of Co_3O_4 nanoparticles onto exfoliated graphite oxide sheets," *J. Mater. Chem.*, **18**, 5625 (2008).
48. S. Aksel and D. Eder,"Catalytic effect of metal oxides on the oxidation resistance in carbon nanotube–inorganic hybrids," *J. Mater. Chem.*, **20**, 9149 (2010).
49. Y. Yao, Z. Yang, H. Sun and S. Wang,"Hydrothermal Synthesis of Co_3O_4–Graphene for Heterogeneous Activation of Peroxymonosulfate for Decomposition of Phenol," *Ind. Eng. Chem. Res.*, **51**, 14958 (2012).
50. S. Chen, J. Zhu, X. Wu, Q. Han and X. Wang,"Graphene oxide-MnO_2 nanocomposites for supercapacitors," *ACS Nano*, **4**, 2822 (2010).
51. S. Navalon, A. Dhakshinamoorthy, M. Alvaro and H. Garcia,"Metal nanoparticles supported on two-dimensional graphenes as heterogeneous catalysts," *Coord. Chem. Rev.*, **312**, 99 (2016).
52. M. Ding, Y. Tang and A. Star,"Understanding Interfaces in Metal–Graphitic Hybrid Nanostructures," *J. Phys. Chem. Lett.*, **4**, 147 (2013).
53. J. Newman,"Current Distribution on a Rotating Disk below the Limiting Current," *J. Electrochem. Soc.*, **113**, 1235 (1966).
54. T. Y. Ma, S. Dai, M. Jaroniec and S. Z. Qiao,"Metal-organic framework derived hybrid Co_3O_4-carbon porous nanowire arrays as reversible oxygen evolution electrodes," *J. Am. Chem. Soc.*, **136**, 13925 (2014).
55. Y. Zhao, S. Chen, B. Sun, D. Su, X. Huang, H. Liu, Y. Yan, K. Sun and G. Wang,"Graphene-Co_3O_4 nanocomposite as electrocatalyst with high performance for oxygen evolution reaction," *Sci. Rep.*, **5**, 7629 (2015).
56. C. Schwanke, H. S. Stein, L. Xi, K. Sliozberg, W. Schuhmann, A. Ludwig and K. M. Lange,"Correlating Oxygen Evolution Catalysts Activity and Electronic Structure by a High-Throughput Investigation of $Ni_{1-y-z}Fe_yCr_zO_x$," *Sci. Rep.*, **7**, 44192 (2017).
57. C. R. Raj, A. Samanta, S. H. Noh, S. Mondal, T. Okajima and T. Ohsaka,"Emerging new generation electrocatalysts for the oxygen reduction reaction," *J. Mater. Chem. A*, **4**, 11156 (2016).
58. R. N. Singh, J. F. Koenig, G. Poillerat and P. Chartier,"Electrochemical Studies on Protective Thin Co_3O_4 and $NiCo_2O_4$ Films Prepared on Titanium by Spray Pyrolysis for Oxygen Evolution," *J. Electrochem. Soc.*, **137**, 1408 (1990).

Tables

Table 1: D to G line (A_D/A_G) integrated area ratios, in-plane crystallite size (L_a). FWHM corresponds to the full width at half-maximum for D and G lines. L_a represents the determined in-plane crystallite size.

	FWHM D (cm^{-1})	FWHM G (cm^{-1})	ν_G (cm^{-1})	A_D/A_G	L_a (nm)
GO	129	58	1589	3.1	5.4
rGO-PR	101	57	1591	2.6	6.3
rGO-SR	69	40	1590	2.2	7.3
Co_3O_4/GO	174	66	1585	3.7	4.5
Co_3O_4/rGO-PR	136	54	1588	3.4	5.0
Co_3O_4/rGO-SR	79	41	1589	2.4	7.0

Schemes

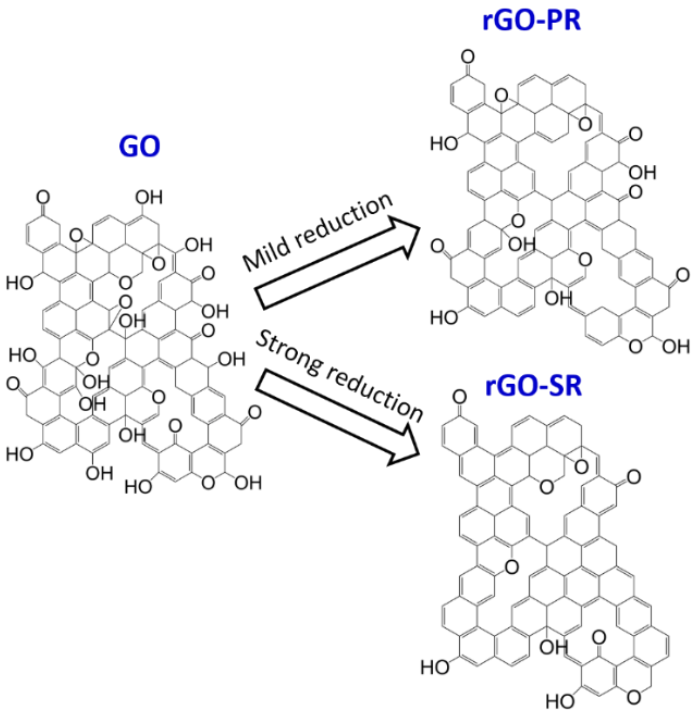

Scheme 1: Illustration of the effect of the reducing treatment on the composition and structure of carbon sheets.

Figures

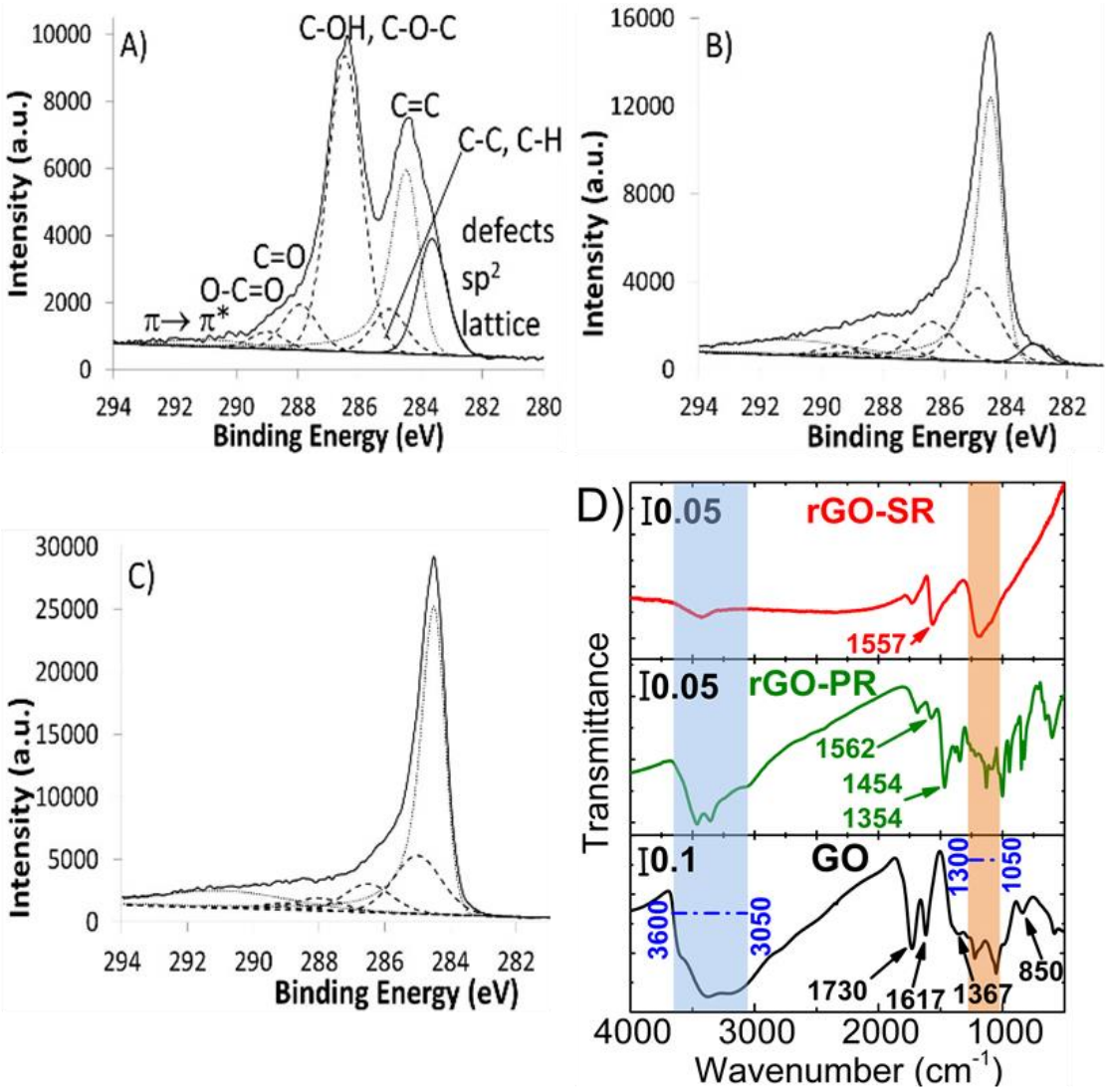

Figure 1: Figure 1: High resolution XPS spectra of C1s region of the different graphene-based materials: A) GO, B) rGO-PR, and C) rGO-SR. D) Transmission FTIR spectra obtained with the different investigated carbon-based materials

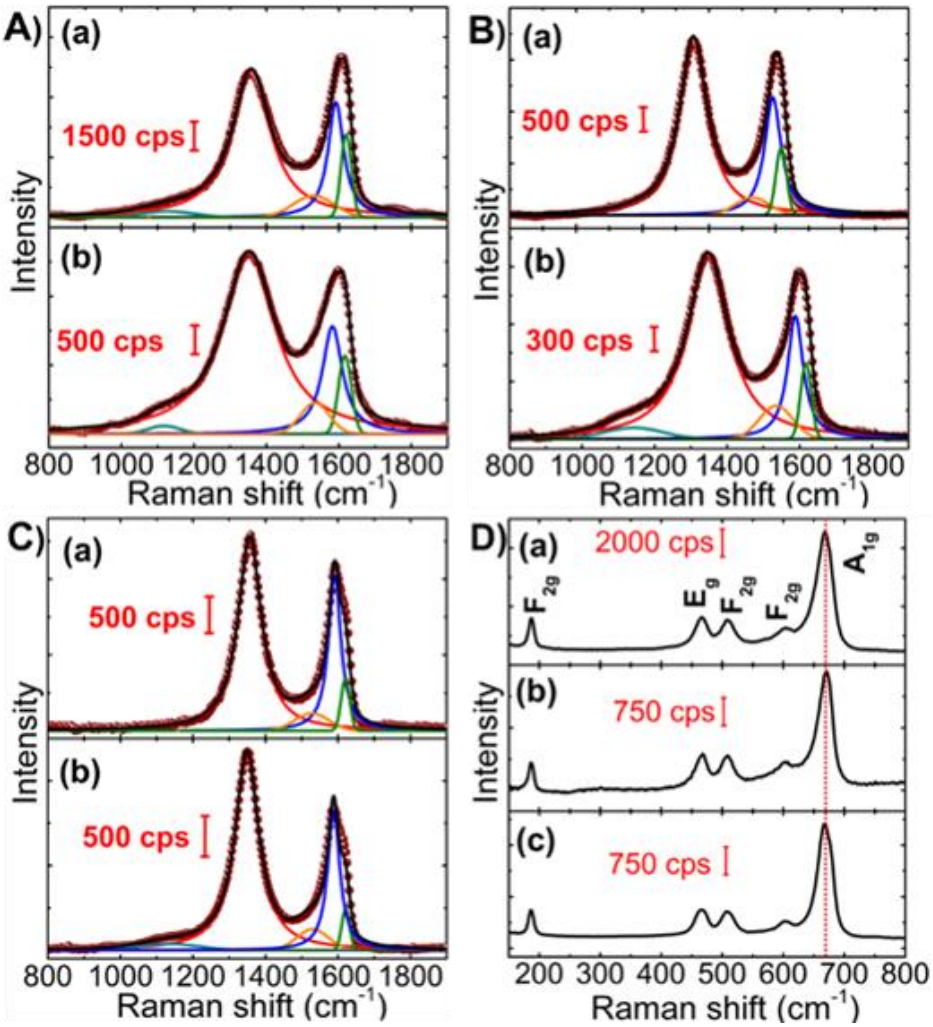

Figure 2: Raman spectra recorded with the different graphene-based substrates: A) GO, B) rGO-PR and C) rGO-SR; (a) without Co_3O_4, (b) after Co_3O_4 deposition. Experimental points are symbolized using brown scatters. Data obtained from decomposition of experimental signals re symbolized using solid lines. D) Raman spectra recorded with the different Co-based nanocomposites: (a) Co_3O_4/GO, (b) Co_3O_4/rGO-PR, (c) Co_3O_4/rGO-SR.

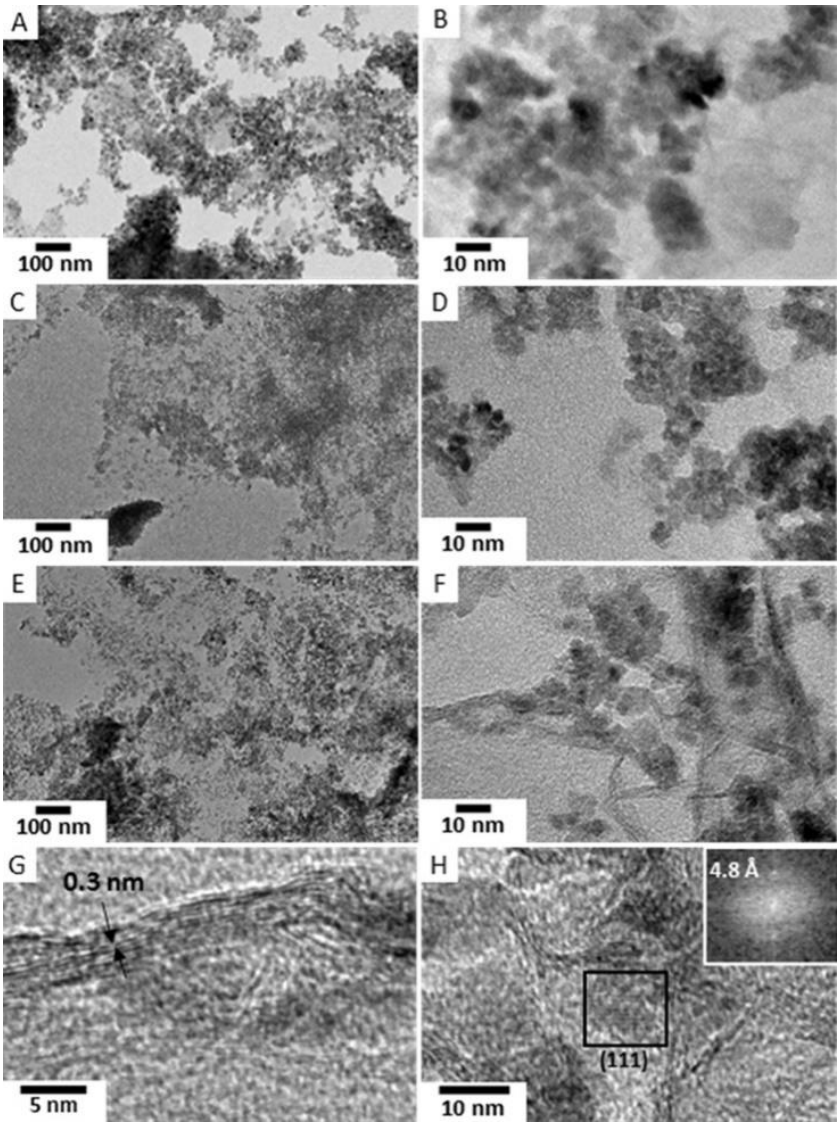

Figure 3: TEM images of the different Co_3O_4/GO and Co_3O_4/rGO nanocomposites: (A, B) Co_3O_4/GO, (A, B) Co_3O_4/rGO-PR, (E-F) Co_3O_4/rGO-SR. Left: low magnification. Right: higher magnification. High resolution TEM images of Co_3O_4/rGO-SR, highlighting (G) an rGO-SR stacked domain, and (H) a Co_3O_4 nanoparticle indexed along the Co_3O_4 structure, inset: FFT of the single particle.

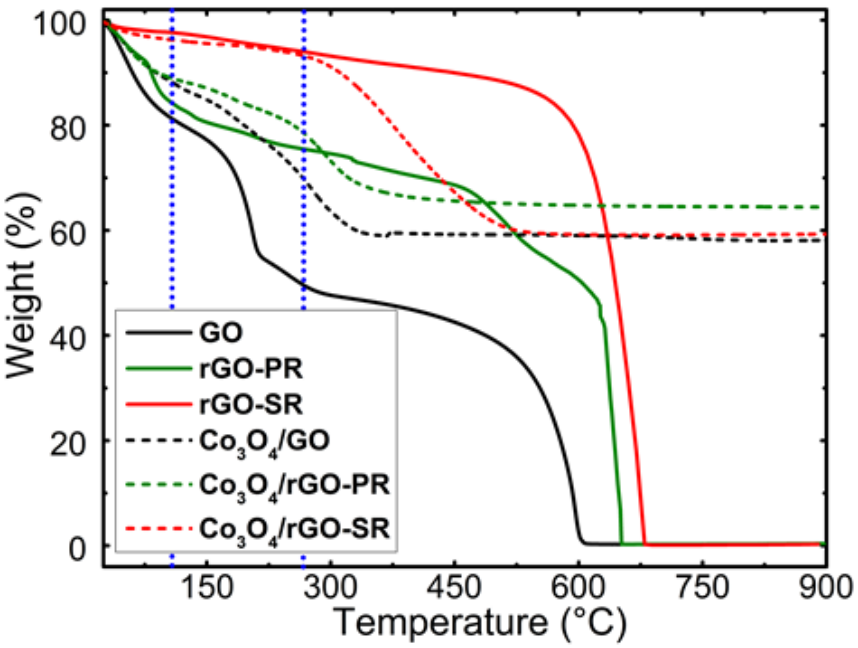

Figure 4: TGA curves recorded under air with the different graphene derivatives and Co-based nanocomposites at heating rate of 10 °C min^{-1}.

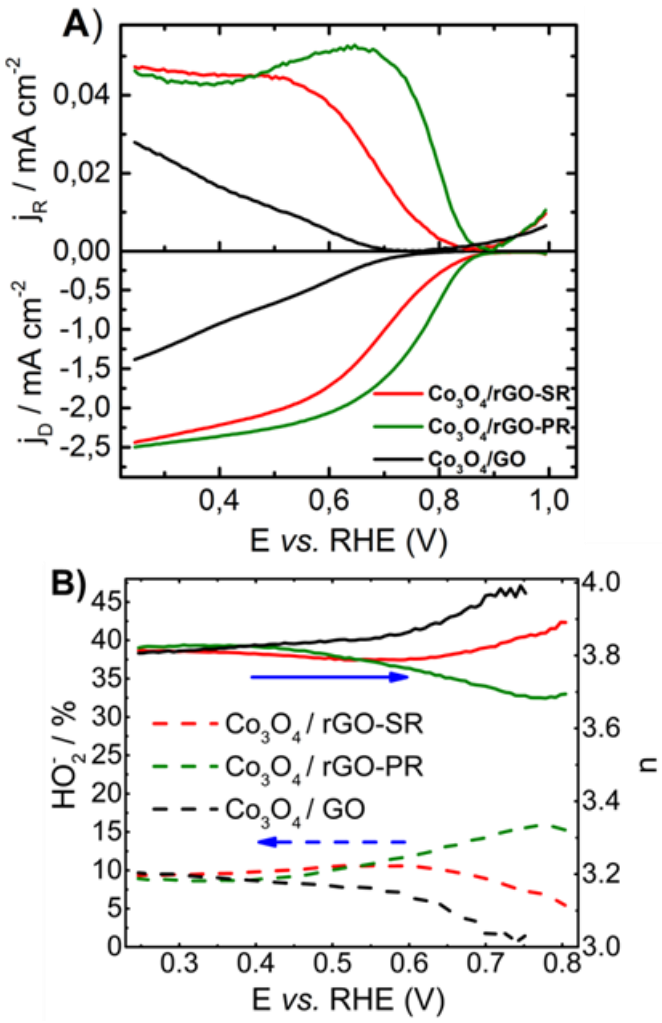

Figure 5: A) ORR polarization curves recorded with the different spinel oxide-based electrocatalysts using a RRDE. These curves were recorded in an O_2-saturated 1 mol L^{-1} KOH solution at a scan rate of 5 mV s^{-1}, at 25 °C and at a rotation rate of 1600 rpm. The ring is polarized at 1.2 V vs. RHE during the experiment. j_R and j_D are currents densities measured with the ring electrode and the disk electrode, respectively. B) Calculated peroxide yield and electron transfer number (nexp) exchanged per oxygen molecule on the basis of RRDE electrochemical data.

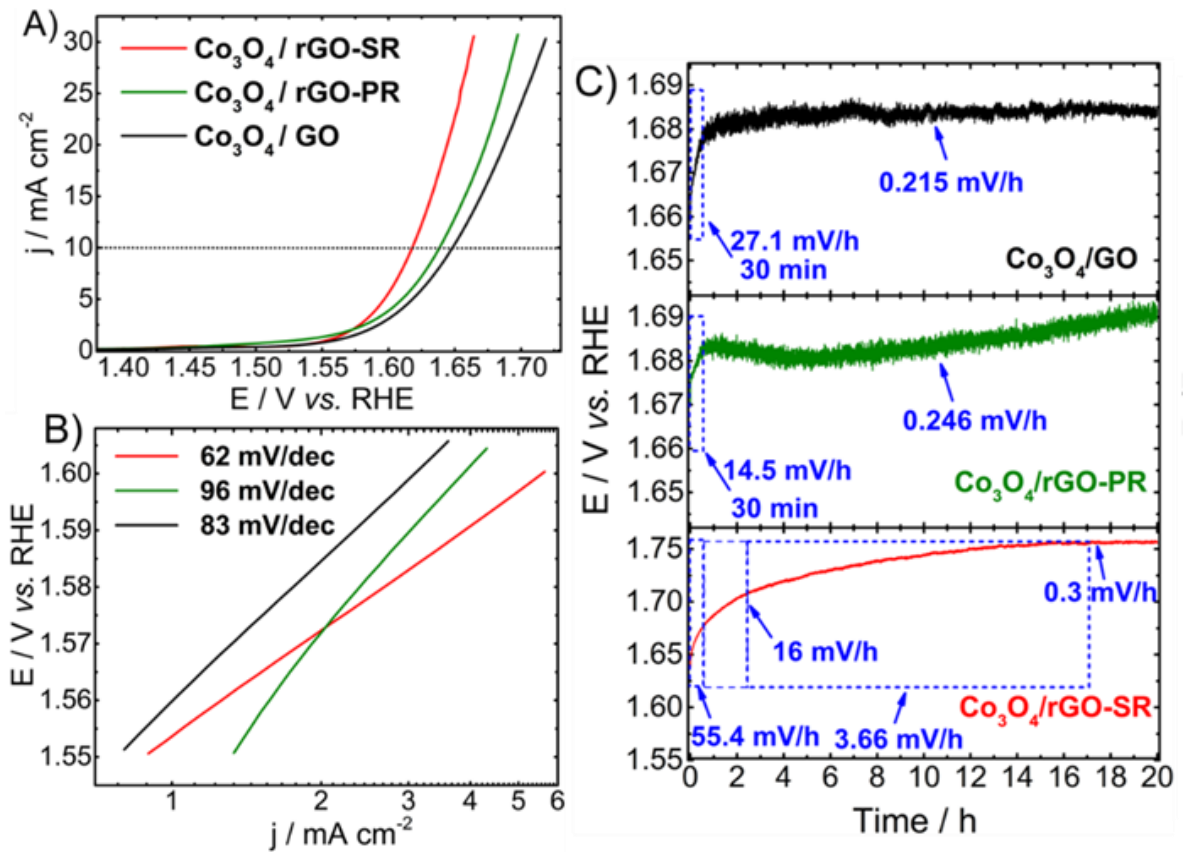

Figure 6: A) Polarization curves in OER conditions obtained with the different Co-based nanocomposites at 1600 rpm at a scan rate of 5 mV s^{-1} in a N_2 saturated 1 mol L^{-1} KOH electrolyte at 25 °C. B) Corresponding Tafel plots. Co_3O_4/rGO-SR (red solid line), Co_3O_4/rGO-PR (green solid line), Co_3O_4/GO (black solid line). C) Chronopotentiometric tests performed with the different Co-based nanocomposites immobilized on a nickel foam. A constant current density of 25 mA cm^{-2} is applied for the test performed in a N_2-saturated 1 mol L^{-1} KOH electrolyte using a home-made air electrode

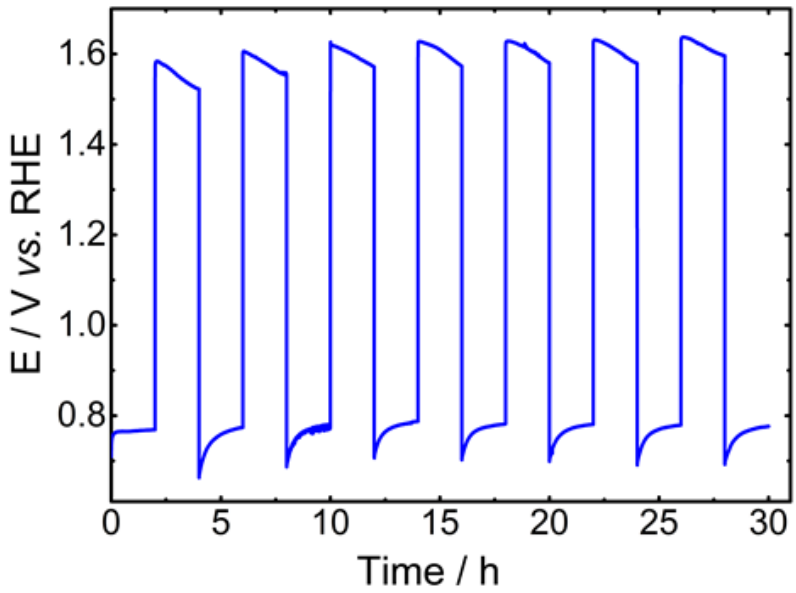

Figure 7: Stability test performed with an air electrode made of the Co_3O_4/rGO-PR catalyst by alternatively applying a current density of -10 mA cm^{-2} during 4 h and a current density of 10 mA cm^{-2} during 4 h. The test is performed at 25 °C in an O_2-saturated 6 mol L^{-1} KOH electrolyte.